Preprint: Higher-Order Modulation for Acoustic Backscatter Communication in Metal

Peter Oppermann
Hamburg University of Technology
Hamburg, Germany
peter.oppermann@tuhh.de

Bernd-Christian Renner
Hamburg University of Technology
Hamburg, Germany
christian.renner@tuhh.de

ABSTRACT

Backscatter communication enables miniature, batteryless, and low-cost wireless sensors. Since electromagnetic waves are strongly attenuated in several scenarios, backscatter communication in metals via acoustic waves can leverage various applications, e. g., in structural health monitoring. When backscattering, the Tag has little control over the modulation it performs on the carrier wave. Therefore, existing approaches commonly employ differential binary modulation schemes, limiting the achievable data rates. To overcome this limitation, we derive a channel model that accurately describes the modulation in an acoustic backscatter channel—as, e. g., found in steel beams—and leverage it to achieve higher-order load modulation. We present an open source Reader and Tag pair prototype based on COTS components that we have developed for communication and on-the-fly channel characterization. We explore the influence of various parameters on communication performance on different channels. Moreover, (i) we are the first to demonstrate that acoustic backscatter is feasible in guided-wave channels, covering up to 3 meters, and that (ii) our modulation scheme achieves up to 211 % higher data rates than binary modulation schemes, and (iii) provides reliable communication through channel coding.

1 INTRODUCTION

During the last decades, radio-frequency identification (RFID) has enabled a variety of IoT applications with very low-cost and low-power wireless sensors using backscatter communication [33]. The core advantage is that sensor nodes can scavenge or harvest energy from carrier waves and modulate the reflected carrier to transmit information passively.

Electromagnetic waves are, however, not viable in every scenario, e. g., underwater or when devices are shielded by metal. Therefore, alternative backscatter-like communication schemes have received wide attention. For example, in-body acoustic backscatter communication can be used in biomedical applications [7, 8, 10] or in underwater marine environments [15], achieving communication distances up to 10 m. Similarly, acoustic power transfer and communication in solids have been proposed for various applications: In structural health monitoring, many testing methods require acoustic transducers that can be reused for communication and wireless power transfer [20]. Sensors within conductive containers, e. g., pressurized tanks, reactors, ship or submarine hulls, cannot be penetrated easily for cable feedthrough [18, 24], even though sensors on the inside need to be powered and read-out. In nuclear facilities, acoustic communication serves as a fallback in emergency situations when radiation renders electromagnetic communication infeasible [11]. Moreover, sensors on airplane wings [17] or in pipelines [31, 32] can use the metallic structure as a medium for communication. We provide an overview of the available approaches to acoustic communication in metals in Sect. 2.1.

Investigations of acoustic backscatter communication in metals have concentrated on short and simple channels and only used binary differential modulation schemes. Multipath characteristics severely affect symbol rates for reliable communication. Higher-order modulation schemes have been shown to increase data rates significantly in electromagnetic [16] and underwater backscatter [1]. Unfortunately, guided-wave metal channels exhibit extreme dependency on geometry, prohibiting the application of the existing approaches with fixed carrier frequencies. We show the potential of using a dynamic, channel-specific carrier in Sect. 5.2.

Our goal is to enable higher-order modulation schemes in metal backscatter channels to increase data rates. This potentially enables applications requiring larger amounts of data, e. g., time series or images, to be transmitted passively. We further demonstrate that dynamic carrier selection at the Reader and adaptive load at the Tag can enhance the SNR of the communication system significantly, in our case up to 37 dB compared to the on average best carrier. For efficient load selection, we leverage a model for the nonlinear acoustic backscatter channel. Furthermore, we aim to develop a practical solution for a wide range of applications, including cheap hardware. Therefore, we have developed a prototype of a Reader and Tag pair, which is able to modulate and demodulate the proposed higher-order modulation. In addition, we sho practical feasibility and merit in a wide range of different channels, i. e., geometries of the structures. We, therefore, present a light-weight protocol for estimating channel parameters in an automated procedure using only the presented

Reader/Tag pair, enabling plug-and-play acoustic backscatter devices. Finally, we present a study showing the feasibility of acoustic backscatter in more complex guided-wave channels and demonstrate, that higher-order modulation in combination with channel coding increases the data-rate in both traditional simple channels as well as in complex channels by up to 211 %.

1.1 Contributions

In summary, we propose and evaluate

- a channel model for the acoustic guided-wave channel,
- a higher-order load modulation scheme,
- a channel estimation procedure,
- a low-cost, open-source Reader and Tag design based on COTS components, and
- a performance study on multiple different channels.

2 ACOUSTIC COMMUNICATION

This section first provides an overview of the related work in acoustic communication through metals by categorizing the existing approaches into four different groups. We then explain the backscatter communication scheme in detail and define the terminology for the rest of this work.

2.1 State Of The Art

A plethora of approaches for communication using acoustic waves in metals have been proposed. However, these approaches have been developed for vastly different environments and are, therefore, not directly comparable. We can distinguish the approaches by two main properties: *active vs. passive* transmitters and the *channel type* in use.

2.1.1 Active and Passive Communication. In active approaches [2, 4, 5, 9, 14, 24, 32, 34], the transmitter actively generates a waveform. This requires power-hungry, analog circuitry but enables the sender to apply any appropriate modulation. Thus, prior work has demonstrated high data-rate communication through metal walls with up to 5 Mbit s^{-1} [24, 34] and usage of modulation schemes with up to 18 bit per symbol.

In passive (backscatter) communication [3, 17, 27, 28, 30], a dedicated device introduces a carrier wave into the medium, and the sender modulates the existing carrier by varying its reflection coefficient. While this implies reduced energy cost and complexity for the passive sender, the control over the resulting waveform is limited. Achievable data rates are much smaller compared to active communication, and are typically in the range of hundreds to a few thousand bits per second. However, data rates of different approaches can only be compared meaningfully when considering the channel.

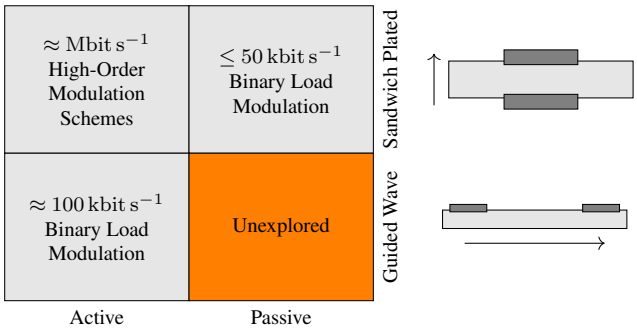

Figure 1: Categorization of previous approaches by means of communication (active vs. passive) and channel in use.

2.1.2 Sandwich-Plated vs. Guided Wave Channel. Most prior work considers a through-wall channel, often also called *sandwich-plated-channel* (SWP), where a pair of transducers is attached concentrically to opposite sides of a metal plate [2, 5, 24, 34] (see Fig. 1). In SWP channels, longitudinal (bulk) waves dominate [25]. In contrast, in a *guided-wave channel* (GW), the transducer pair is attached at arbitrary locations on the surface of a plate-like metallic structure, either on the same or on opposite sides.

Both channel types have different characteristics. Much shorter symbol times are achievable in SWP channels compared to GW channels, allowing for higher data rates. The longitudinal waves in SWP channels propagate faster and can be efficiently excited in a broad range of frequencies. In GW channels, transversal (lamb) waves propagate most effectively, and are best excited in a limited frequency range where the wavelength is in the order of magnitude of the thickness of the plate-like structure [29]. This can be observed in Figure 2, showing the magnitude of the channel response to a short sine burst for an SWP and a GW channel on the same specimen. The GW channel response peaks around 200 kHz, and for higher frequencies, the magnitude drops significantly. The SWP, in contrast, additionally shows a strong response in higher frequency ranges above 1 MHz. In this experiment, the piezo disks have their radial and thickness resonance at 200 kHz and 1 MHz, respectively.

Additionally, lamb waves propagate slower and experience less attenuation, resulting in stronger reverberation. This can be observed in Fig. 3, where the power delay profile of burst responses is displayed in the different frequency ranges. The delay spread in the low-frequency range is much larger than in the high-frequency range, and the amplitudes in the high-frequency range are negligible in GW channels.

Matching these observations, prior work on GW channels achieved significantly lower data rates of just a few hundred

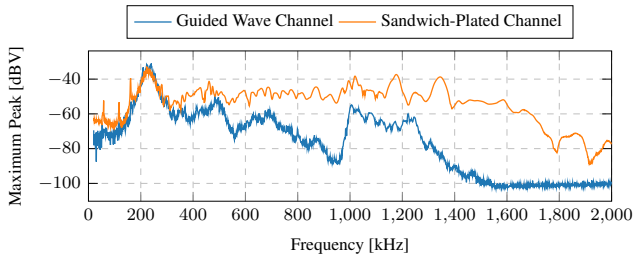

Figure 2: Highest amplitude after burst excitation in different channel types.

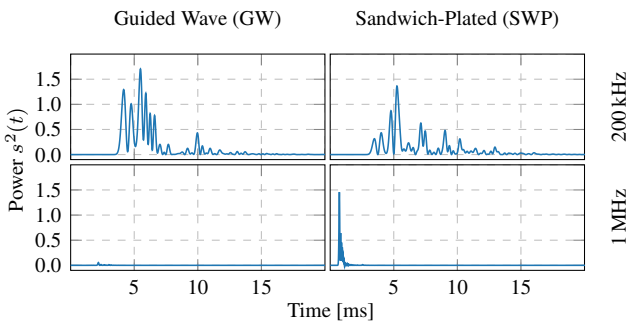

Figure 3: Power of channel responses $s(t)$ to a short excitation pulse at different frequencies. Sandwich-Plated channels allow for higher carrier frequencies, which, in turn, show much less reverberation.

to a few thousand bits per second even with active communication [4, 13, 14, 32]. The highest data rates in passive SWP reach 55 kbit s^{-1} [28] in a thick (5 cm) block while reaching 2.7 kbit s^{-1} in thin (3 mm) plates [6].

To the best of our knowledge, no passive communication in GW channels has been presented yet and higher-order modulation has not been used either in passive communication in metals. However, in conventional electromagnetic and underwater backscatter, higher-order modulation has already been investigated. In these scenarios the Reader is configured to only generate a fixed carrier frequency that depends solely on the transducer's resonance. The loads at the Tag are therefore also fixed, because their optimal choice depends only on the piezo's source impedance and the carrier frequency. That is sufficient in environments, where Reader and Tag are typically mobile and hence, channels are highly volatile. In contrast, the transducers in the metal channel are fixed to the structure and, hence, the channel is static, but highly frequency dependent. It is therefore promising to adapt the carrier frequency of the Reader to the specific channel to maximize the SNR of the communication. However, with dynamic carrier frequency, no single set of loads at the Tag is able to produce the optimal constellation points

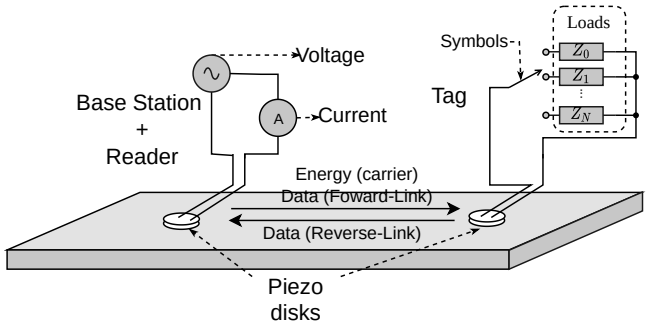

Figure 4: The typical RFID system consists of three devices: Base Station, Reader, and one or more Tags. Base Station and Reader are often combined in one physical device, even sharing the same transducer. In our case, the transducers are piezoelectric discs.

for the channel, and hence, a more flexible load impedance choice has to be implemented in the Tag.

2.2 Backscatter Principle

Backscatter communication is well known from *Radio-Frequency Identification* (RFID), as used in, e. g., smartcards, contactless payments, and near-field communication (NFC). Despite the different physical wave types—acoustic and electromagnetic waves—the basic principles are the same, and we adopt the terminology from RFID as described in [22, p.12ff].

A backscatter communication system consists of three elementary parts (Fig. 4). First, there is the *Tag*, which passively transmits information by modulating the load at its transducer. It relies on a *Base Station* to generate the sinusoidal carrier wave in the medium. The Base Station can optionally modulate the carrier to transmit information to the Tag (*forward-link*), which is conceptually simple because the Base Station fully controls the generated waveform and the channel is linear, e. g., doubling the waveform's amplitude will also double the the received signal at the Tag. Exemplarily, the authors of [20] have described a pulse-based acoustic sender and receiver with an envelope detector. We will not focus on the forward link in the remainder of this work.

The third element is the *Reader*, which demodulates the Tag's signal (*reverse-link*). The impedance of the transducer at the Reader is influenced by the load at the Tag due to an electromechanical coupling. However, the effect of different loads on the Reader's measurement is subtle and nonlinear, e. g., doubling the load impedance may change the observed impedance at the Reader arbitrarily, depending on the exact channel. Prior work in acoustic communication has focused on binary and differential load modulation, where the Tag

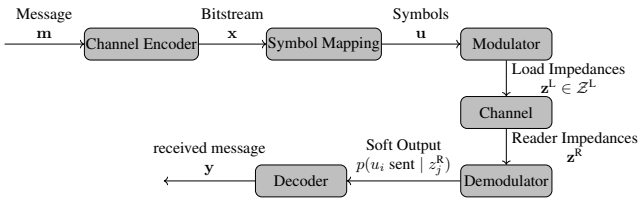

Figure 5: A block diagram showing the basic elements of the communication system and the notation of the different vectors used to describe it.

switches between only two states, often realized with a transistor switching between open and closed state. As we aim to implement higher-order modulation, the Tag must be capable of choosing from more than two impedances.

3 ACOUSTIC BACKSCATTER COMMUNICATION

We present the basic elements of our communication system and discuss the required channel information. We then elaborate on the properties of the acoustic metal channel and describe a channel model, including the structural and electric components of the channel. This model is needed to choose appropriate loads at the Tag, so that the Reader can distinguish between different symbols reliably. We validate the model using experimental data in Sect. 5.3.

Figure 5 shows the elementary parts of our communication system and the notation of the information vectors used in this article. The presented system implements block-based communication. The Tag first encodes a block of message bits $\mathbf{m}$, where additional bits are appended for forward error correction (FEC). We use low-density parity-check (LDPC) codes with short block sizes because encoding can be done with reasonable effort, and most effort is shifted to the decoder, which suits the typical applications of backscatter networking, where Tags are constrained low-power devices and intense computation must be offloaded to the Reader.

The resulting bitstream is mapped on a set of S symbols, where each block of $\log_2(S)$ bits is mapped to one symbol. Then, the Tag applies a unique load impedance z^{L} from the set of all selectable loads $\mathcal{Z}^{\mathrm{L}} = \{z^{\mathrm{L},1}, \ldots, z^{\mathrm{L},S}\}$ at its transducer for each symbol.

The impedance of the Reader's transducer depends on the load at the Tag's transducer and there is a unique mapping between $\mathcal{Z}^{\mathrm{L}} \to \mathcal{Z}^{\mathrm{R}}$, where $\mathcal{Z}^{\mathrm{R}}$ is the set of corresponding impedances at the Reader. The Reader observes the impedances over time and can calculate the likelihoods of the selected symbols at the Tag. Using this soft channel information, the decoder determines the most probable message $\mathbf{y}$.

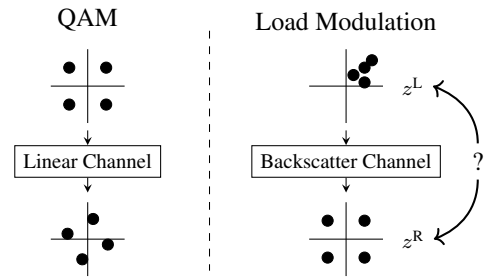

Figure 6: In classical communication, linear channels preserve the relative positioning between symbol constellation points. This relationship is nonlinear in the backscatter channel with load modulation and must be determined to select suitable symbols.

3.1 Steady-State Channel Model

In contrast to conventional wireless communication channels, the backscatter channel is nonlinear, i. e., the mapping $z^{\mathrm{L}} \to z^{\mathrm{R}}$, is a nonlinear function. For optimal choice of $\mathcal{Z}^{\mathrm{L}}$, this mapping must be known. Our goal is to choose the load impedances such that the symbol constellation points observed by the Reader are most distinguishable, i. e., the minimum of the pairwise distances between constellation points is maximized. In QAM, for example, the sender uses evenly distributed constellation points in the signal space (Fig. 6), and in a linear channel, the received symbols will then also be distributed evenly. With load modulation, however, the nonlinear relation between load and observed impedance must be known to select the load impedances so that the observed constellation points are also evenly distributed. A model of the channel is required to predict this relation.

In steady-state, the electromechanic system can be represented by an equivalent electrical circuit [26]. In such an equivalent circuit, the concept of acoustic impedance is used analogously to that of electrical impedance, where voltage v and current i represent mechanical pressure and particle velocity. This has two advantages: The system can be analyzed with electrical engineering methods, and the behavior of the electrical and mechanical components can be combined in a single model.

A typical equivalent circuit that has been used for a system of two piezo transducers attached to a metallic structure is the Butterworth-van Dyke lumped element model shown in Fig. 7 (left) [30, 31]. The model includes the electric impedances of the piezo transducers at Tag and Reader ($R_{\mathrm{T}}^{\mathrm{e}}$, $C_{\mathrm{T}}^{\mathrm{e}}$, and $R_{\mathrm{R}}^{\mathrm{e}}$, $C_{\mathrm{R}}^{\mathrm{e}}$) as well as the acoustic equivalent impedance of the metal channel (R_{m}^{i}, L_{m}^{i} and C_{m}^{i}). Every parallel branch is equivalent to one resonant mode of the structure. If excited with a resonant frequency, the L and C components of that

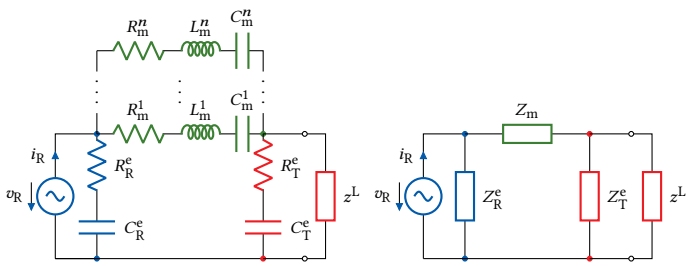

Figure 7: Butterworth Van-Dyke lumped element model for the metal channel. Adapted from [31] (left), and simplified for only a single frequency (right). The components corresponding to the Reader (blue), Channel (green), and Tag (red).

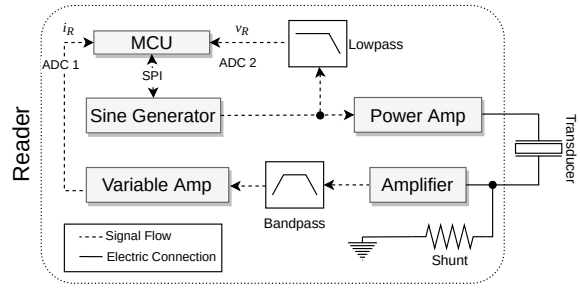

Figure 8: Block diagram of the Reader signal processing chain.

branch cancel out each other, and the channel's impedance reaches a local minimum.

The values of the RLC elements representing the metal channel are generally unknown, but could be determined using a 2-port network analyzer [31]. For plug-and-play like deployability we have to be able to estimate the channel with our low-cost Reader and Tag hardware. Since we use only a single carrier frequency for transmission, we can simplify the diagram as in Fig. 7 (bottom) by combining all parallel paths to a constant complex impedance.

Acoustic backscatter communication relies on the measurement of the impedance z^{R} at the Reader's transducer. Therefore, we apply the known sinusoidal voltage v_{R} at the transducer's terminals and measure the resulting current i_{R}. Using the equivalent circuit, we can analytically derive the Reader's impedance depending on the load z^{L} at the Tag as

$$z^{\mathrm{R}} = \frac{u_{\mathrm{R}}}{i_{\mathrm{R}}} = \frac{z^{\mathrm{L}} \cdot (Z_{\mathrm{R}}^{\mathrm{e}} Z_{\mathrm{m}} + Z_{\mathrm{R}}^{\mathrm{e}} Z_{\mathrm{T}}^{\mathrm{e}}) + Z_{\mathrm{R}}^{\mathrm{e}} Z_{\mathrm{m}} Z_{\mathrm{T}}^{\mathrm{e}}}{z^{\mathrm{L}} \cdot (Z_{\mathrm{R}}^{\mathrm{e}} + Z_{\mathrm{m}} + Z_{\mathrm{T}}^{\mathrm{e}}) + Z_{\mathrm{T}}^{\mathrm{e}} (Z_{\mathrm{R}}^{\mathrm{e}} + Z_{\mathrm{m}})} \,. \tag{1}$$

The resulting transformation from z^{L} to z^{R} is a Moebius transformation: a rational function in the form

$$z^{\mathrm{R}} = \frac{z^{\mathrm{L}} a + b}{z^{\mathrm{L}} c + d} \,, \tag{2}$$

where $a, b, c, d \in \mathbb{C}$. The bijectivity of this transformation guarantees a unique z^{R} for every z^{L}.

The values a, b, c and d can be determined analytically with three known points $(z_i^{\mathrm{R}}, z_i^{\mathrm{L}})$, $i \in \{1, 2, 3\}$. We can, therefore, characterize the transformation for a specific frequency by observing the impedances z^{R} with three different loads, and then pick the desired constellation points at the Reader. This will be used during the channel estimation procedure described in Sect. 4.3.2.

4 IMPLEMENTATION

Next, we present a hardware prototype for Reader and Tag. Our goal was to develop a proof of concept using affordable, off-the-shelf components to enable other researchers to copy and adapt the platform for their own experiments. We will publish all sources and material under a permissive open-source license. A limitation of this approach and component shortage on the market, the prototype is not yet optimized for ultra low-power demands.

4.1 Reader Hardware Design

The Reader must fulfill two main tasks: Generating a carrier with selectable frequency, and measuring the impedance of its transducer. The sine wave is generated using the AD9833 waveform generator IC from Analog Devices. This IC uses Direct Digital Synthesis to produce a sinusoidal output. The generated sine wave is amplified up to 25 V peak-to-peak amplitude before it is applied to a piezo transducer.

Assessing the impedance of the Reader requires knowledge of the transducer current and voltage. The current is measured at the low side of the transducer using a small 3 Ω shunt resistor in series with the transducer. The voltage drop across the shunt resistor is amplified and filtered with a 4th-order bandpass filter to reduce noise. the resulting signal is proportional to the current flow through the transducer. The setup is shown schematically in Fig. 8.

An STM32F446 microcontroller is used to sample both the generated voltage and the current through the transducer with its onboard Analog-to-Digital (ADC) converters. The samples are processed directly by applying a short-term Fourier transform (STFT). We compute the transducer's impedance as

$$z^{\mathrm{R}} = A_{\mathrm{v}} / A_{\mathrm{i}} e^{j \Delta\phi}, \tag{3}$$

where A_{v} and A_{v} are the amplitudes of voltage and current measurements, and $\Delta\phi$ is their phase difference.

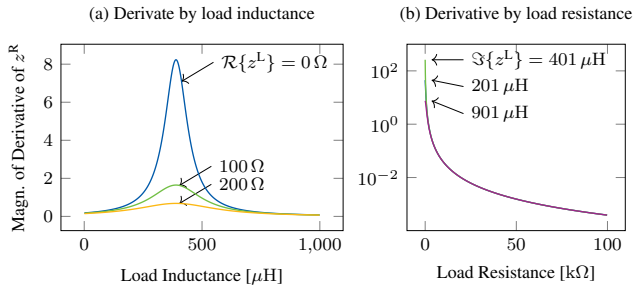

Figure 9: Magnitude of derivative of z^R over changes in load impedance with typical parameters for Eq. (1) ($R^e_R = R^e_T = 10\,\Omega$, $C^e_R = C^e_T = 1\,$nF, $Z_m = (1 - j)$kΩ) at carrier frequency 220 kHz.

The generated frequency, the sampling rate, and the number of samples per impedance measurement have to be carefully selected to avoid leakage effects during the application of the STFT.

4.2 Tag Hardware Design

The Tag's circuit, depicted in Fig. 10, must be capable of applying a range of different impedances to its transducer. A free choice of resistance and reactance is optimal, although not practially achievable. To investigate the required range of load impedances, we investigate the derivative of the observed impedance at the Reader when changing the resistance or inductance of the load at the Tag. Figure 9 (a) shows, that the influence of the inductance is largest close to the resonance, while (b) shows, that the largest influence of resistance occurs in low resistances.

For a digitally controlled resistance, we use a digital potentiometer, which has a low wiper resistance. At the same time, we require high resolution, especially in the low-resistance range. We therefore decided for the AD5175, a 1024-step 10 kΩ potentiometer with a 50 Ω wiper resistance.

Due to the lack of digitally controlled inductors, we use a set of fixed inductors in parallel, and analog switches to activate or deactivate them. We require switches with small on-state resistances (≈ 1 Ω) to not increase the minimal achievable resistance significantly, which is dominated by the wiper resistance of the potentiometer. The reactances must be chosen carefully for maximum SNR. In Figure 9 (a), peak influence on z^R occurs when the inductances match the capacity of the piezoelectric transducer, which is given in its datasheet. The selected inductors should be distributed around the exact matching inductance. If the carrier frequency was fixed, ideal inductances could be calculated. However, with variable carrier and limited commercial availability of component values, we can not choose ideal inductors.

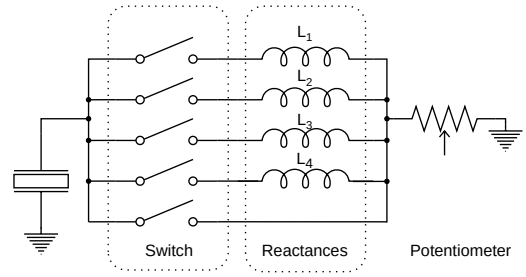

Figure 10: Schematic Diagram of the Tag's modulation circuit.

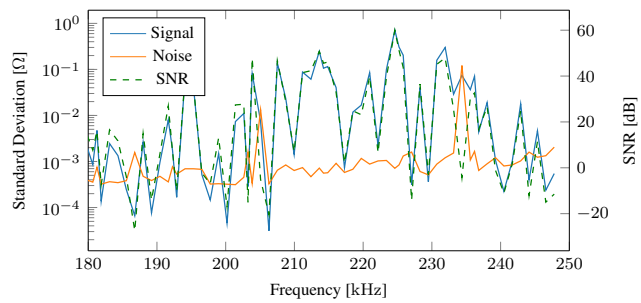

Figure 11: Standard deviation of the observed impedance at the Reader at different frequencies. The Tag is constantly modulating its load impedance while the Reader measures the signal. The noise level is determined while the Tag is not modulating.

4.3 Calibration Procedure

Before Tag and Reader can communicate, they have to calibrate, i. e., first pick a suitable carrier frequency, and then, the best $\mathcal{Z}^L$ have to be determined. Lastly, the Reader has to *learn* the mapping between the applied symbol u and the expected impedances $\mathcal{Z}^R$. Examples from a real channel are used to illustrate the process, the experiment setup used to generate them is described in Sect. 5.

4.3.1 Carrier Frequency Selection. We aim to find a frequency, at which the modulation of the load z^T produces the largest change of the observed impedance z^R. The frequency response of the channel depends on many factors and is very sensitive to small changes—e. g., slightly different placement of transducers. Hence, it is not practical to determine it with simulation, as attempted in [25]. Therefore, the best frequency is determined experimentally. With ~30 s, this is the most time- and energy-consuming task during calibration. However, throughout experiments over several weeks, we observed that the optimal frequency does not change much with varying environmental conditions and, hence, has to be determined only once when Reader and Tag are placed.

In this calibration stage, the Tag switches through a set of different loads while the Reader performs a frequency sweep. For ever freqeuncy, it measures the transducer's impedance long enough to observe all the different load states generated by the Tag. The standard deviation of the observed impedances is taken as metric for the resulting signal intensity for each frequency. Together with the noise level, the SNR can be calculated. The Reader then picks the frequency with largest SNR. Figure 11 shows the result for an exemplary channel. A more detailed analysis of frequency response variations between channels is provided in Sect. 5.2.

4.3.2 Choosing load impedances. In the next step, the Reader determines the mapping between symbols and load impedances. Our Tag with 5 reactance states and a 1024-step potentiometer can produce more than 5000 different loads. Simply testing all of them is time and energy consuming. Alternatively, we leverage the knowledge that the mapping between the load state at the Tag and the observed load at the Reader is a Moebius transformation.

The Tag sends a pilot sequence by selecting three different resistances for each reactance state, while the Reader observes the resulting impedances. From these three points, the Tag can compute the transform and estimate z^{R} for every possible load. Figure 12 (left) shows the estimated transformations for a specific channel.

The Reader then picks the loads $z^{\mathrm{L},i}, i \in [1, 2, \ldots, S]$ such that $\min_{i,j,i\neq j} \left\| z^{\mathrm{R},i} - z^{\mathrm{R},j} \right\|$ is maximized. The Reader then uses the forward-link to inform the Tag about the chosen set $\mathcal{Z}^{\mathrm{L}}$ for each symbol. Figure 12 (right) shows the selected loads based on the transformation. For evaluation purposes, we measured the real z^{R} for every selected $z^{\mathrm{L},i}$ and compared it to the prediction.

4.3.3 Channel Estimation. The estimate of the Moebius transformation is accurate enough to pick unidistantly spaced loads, but they do not perfectly match the observed impedances, as Fig. 12 (right) shows. Furthermore, the exact values slightly vary over time due to changes in ambient conditions, such as temperature. Accurate knowledge of constellation points is, however, required for communication. Hence, a channel estimate has to be performed repeatedly, in which the Reader updates $z^{\mathrm{L}} \rightarrow z^{\mathrm{R}}$.

In the channel estimation step, the Tag sends a pilot message, in which it switches through all $z^{\mathrm{L},i}$. From this message, the Reader can obtain the exact $z^{\mathrm{R},i}$. Because of the long delay spread in the metal channel, a long symbol duration of ~ 20 ms is used at this stage to allow the channel to converge to steady state for each symbol.

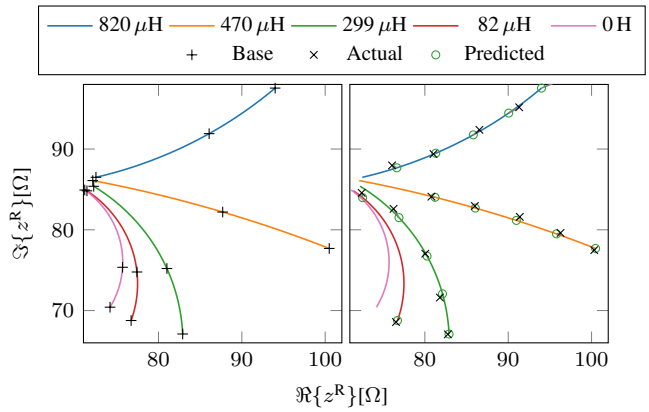

Figure 12: The estimated transformations based on just three measurements per reactance (left). Every branch shows the range of impedances that can be generated when keeping the Tag's reactance fixed and only change the resistance. In this example, 16 loads are picked, such that they are uniformly distributed in the complex impedance plane (right).

4.4 Communication System

In the previous section, we have established the loads and estimated the channel. This section explains the packet-based transmission scheme. First, we present the packet structure and encoding process in the Tag, then we move to the reception at the Reader. Finally, the demodulation of soft channel outputs for decoding is explained.

4.4.1 Sending. The message bits $\mathbf{m}$ are encoded with an LDPC code, where redundant parity bits are added to the message. The code rate R describes the ratio of payload bits to total transmitted bits. The encoded bitstream $\mathbf{x}$ is then converted to a stream of symbols. We use a grey code so that adjacent symbols only differ in a single bit, which reduces the number of bit errors because, in case of an error, a symbol is most likely confused with its direct neighbor.

Finally, the Tag adds a preamble for synchronization consisting of three symbols. The symbols are then sent by applying the appropriate load impedances, where each symbol lasts for a symbol period of T_s.

4.4.2 Synchronization and Channel Adaption. The Reader continually takes impedance measurements. Using the known preamble sequence and the mapping from symbols to constellation points, it generates a preamble correlation signal. The preamble serves two purposes: The Reader detects the start of a message, once the correlation exceeds a threshold, and the observed impedances during the correlation are used as a training sequence to refine the channel estimation.

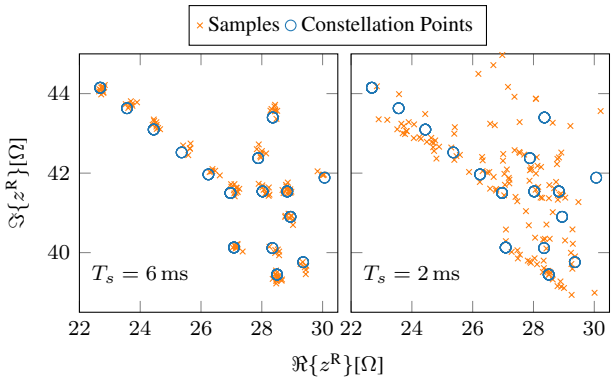

Figure 13: Samples and respective constellation points. With long symbol times (left), inter-symbol interference is small and samples cluster at constellation points. With short symbol times (right), samples deviate notably from constellation points.

Small changes in these impedances caused by ambient influences can change the mapping $z^L \rightarrow z^R$ significantly. However, we can use the observed preamble to correct these variations: Assume that at the time of the channel estimation, the channel was described by the Moebius transform w. In the meantime, the channel has changed slightly and is now described by $\tilde{w}$. This implies, that a third Moebius transform exists which maps $w \rightarrow \tilde{w}$, and this transform can again be determined by three known points. We can use the preamble for this purpose, since it provides three symbols, where we know which impedance we would have expected under the old transform w, and which we have actually measured under the current transform $\tilde{w}$. With this new transform, we can update our symbol constellation points at the Reader accordingly. The effects of this adaption are evaluated in Sect. 5.6.

4.4.3 Sampling and Decoding. After preamble detection, the Reader samples the payload impedances. After every symbol transition, the channel shows transient behavior before converging to a new steady-state. Hence, the sampling rate must be several-fold higher than the symbol rate during synchronization. Once the preamble has been detected, the samples for the payload only need to be taken once towards the end of each symbol duration, when the channel has converged to a steady state. This yields the demodulated signal $\mathbf{z}^R = [z_0^R, z_1^R, \cdots, z_N^R]$. Figure 13 shows the samples when taken 2 ms and 6 ms after symbol transition. The influence of ISI is clearly visible.

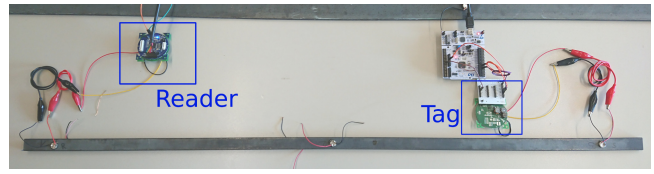

Figure 14: Setup with Tag and Reader. Their transducers are attached to a steel specimen with a length of 1 m.

To decode an LDPC code, we must determine log-likelihood ratios (LLR) for each bit. The LLR [21] is defined as

$$\mathrm{LLR}(x_j \mid z_i^R) = \log \frac{\mathrm{p}(z_i^R \mid x_j = 0)}{\mathrm{p}(z_i^R \mid x_j = 1)} + \log \frac{\mathrm{p}(x_j = 0)}{\mathrm{p}(x_j = 1)}. \quad (4)$$

Without prior knowledge of the sent message, the a priori probabilities of a sent bit being one or zero are assumed equally likely and the second term can hence be discarded. The probability of an observed impedance given a single transmitted bit is

$$\begin{aligned} \mathrm{p}(z_j^R \mid x_j = 0) &= \frac{\mathrm{p}(z_j^R, x_j = 0)}{\mathrm{p}(x_j = 0)} = \frac{\sum_k \mathrm{p}(z_j^R, u_k)}{\mathrm{p}(x_j = 0)} \\ &= \frac{\sum_k \mathrm{p}(z_j^R \mid u_k)\mathrm{p}(u_k)}{\mathrm{p}(x_j = 0)} \\ &= \frac{2}{S} \sum_k \mathrm{p}(z_j^R \mid u_k), \end{aligned} \quad (5)$$

where k loops over all symbols in which the j-th bit is zero. The probability $\mathrm{p}(z_j^R \mid x_j = 1)$ is constructed analogously. The last equality follows from the assumption of equally likely symbols, we assume $\mathrm{p}(u_k) = 1/S$ and $\mathrm{p}(x_j = 0) = 1/2$.

Assuming Gaussian noise with zero-mean and standard deviation σ,

$$\mathrm{p}(z_j^R \mid u_k) = \frac{1}{\sqrt{2\pi}\sigma} \exp\left(-\frac{\|z_j^R - z^{R,k}\|^2}{2\sigma^2}\right). \quad (6)$$

With the LLRs for each bit, belief-propagation decoding is performed, and the redundant parity bits are removed, leaving only the decoded information bits.

5 EVALUATION

Next, we describe the evaluation setup and investigate the proposed channel model and resulting load selection algorithm. We then explore the maximum achievable data rates with different parameters, i. e., the number of symbols, the effect of the refined channel estimates, and the coding gain.

5.1 Evaluation Setup

In the following experiments, we have used the Tag and Reader hardware described in Sect. 4. To be more flexible in parameter choice, we chose to run part of the processing on a desktop computer (PC), which was connected to the Tag and Reader via a serial interface. More specifically, the PC configures the load impedances per symbol (z^{L}), while the Reader transmitted impedance measurements (z^{R}) to the PC. In a real application, the Reader would process the samples completely on its MCU.

The piezoelectric transducers were attached to two different specimens using epoxy resin to achieve a strong coupling with the metal. In total, we used five distinct channels to ensure our method works in various scenarios: One SWP and four GW channels with transducers 1 m (GW1), 2 m (GW2) and 3 m (GW3) apart on a 3.5 m × 5 cm × 0.5 cm steel beam. The last channel (GW4) is a GW channel on a smaller steel beam with dimensions 1 m × 2 cm × 1 cm. The disk-shaped transducers have a diameter of 1 cm and a thickness of 2 mm. According to the specification, their resonant frequency in radial mode is 200 kHz and 1 MHz in thickness mode.

5.2 Dynamic Frequency Selection

In conventional backscatter scenarios, a fixed carrier frequency is selected. We want to quantify the gain of a dynamic adaption of the carrier frequency in metal channels. Figure 15 shows the SNR over frequency acquired for three channels on the same specimen. For every channel, the measurement was repeated ten times and the average is shown. The standard deviations between the SNRs in the ten repetitions was approximately 3 dB in all channels. The SNR varies strongly and can change more than 40 dB within just 1 kHz. Further, there is no single frequency that performs optimal in all three channels.

Even if, in a fixed carrier scenario, we select the carrier that performs best on average over all three channels (228 kHz, average taken over the SNRs in dB), this carrier is not optimal for any channel. For channel GW1, a better carrier exists that has 15 dB higher SNR, while channels GW2 and GW3 can onl slightly be improved by 2 dB, or 3 dB respectively. An unlucky pick in the carrier frequency, e. g., 227 kHz would perform 70 dB worse than the optimum in GW1, and 48 dB worse than the optimum in GW2. Note that the three channels are recorded on the same specimen with the same transducers. The only difference between them is the placement of the transducers. For plug-and-play Reader and Tags, dynamic frequency selection is expected to strongly increase the performance.

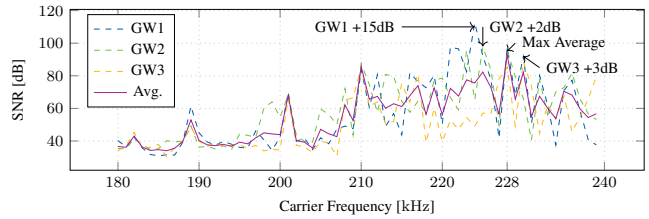

Figure 15: Signal to Noise ratio over carrier frequency in different channels. Picking an individual carrier frequency for each channel increases SNR.

5.3 Dynamic Load Picking

This section investigates the tradeoff between fixed loads, as commonly used in backscatter systems, and dynamically picked loads, as proposed in this work. One advantage is the reduced need for components, especially bulky inductors. Using dynamic load picking, inductors can be reused for several constellation points or combined in parallel branches by activating multiple switches simultaneously. In contrast, with fixed loads, each load requires its own inductor. Furthermore, optimal loads may require unrealistically dimensioned components, i. e., large inductors in the range of tens to hundreds of millihenries.

The modulation range is the set of all z^{R} that can be produced with arbitrary loads at the Tag. It is represented by a circle, where $\Re\{z^{\mathrm{L}}\} = 0$. With the presented Tag, however, the minimum resistance is constrained by the wiper resistance of the potentiometer—at least 50 Ω. This reduced the modulation range to a smaller circle (See Fig. 16, left). To quantify this reduction, we evaluated the unconstrained radius with zero resistance, i. e., with the potentiometer short circuited. Then we repeated the measurements with the potentiometer in the loop(constrained). The use of the potentiometer reduced the modulation range of the impedances by 7 % on average over all channels and carrier frequencies under test. The minimum radius reduction was 3.4 % and the maximum 12 %.

Important for the performance of the communication is the minimum distance between any two constellation points, as formulated in Sect. 4.3.2. The presented Tag is limited to a set of inductors and the range of the potentiometer. Figure 16 (right) compares the optimum minimal distances for all channels with unconstrained load picking versus the constrained minimal distances. In some channels, the distances are nearly halved, while in others, especially with just 2 symbols, the range is hardly reduced at all.

Unsurprisingly, unconstrained loads perform better. To decide if dynamic loads are favourable over fixed loads, we now investigate if there is a single set of fixed, arbitrary loads, that outperforms the constrained loads in all channels,

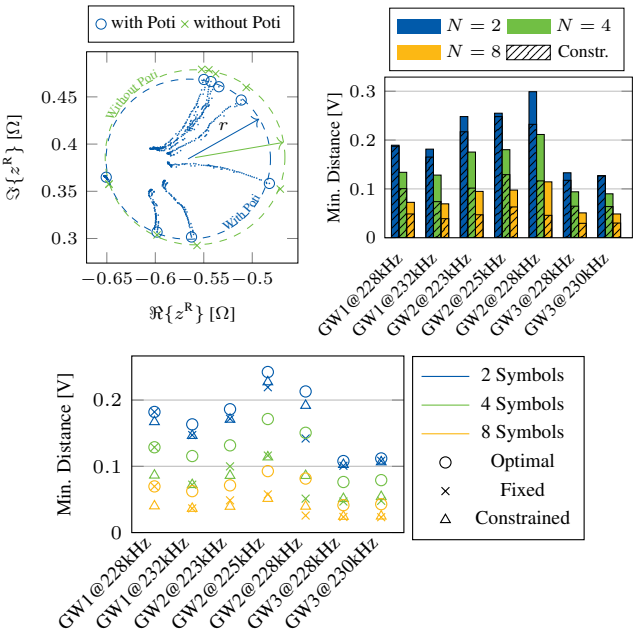

Figure 16: The modulation range is constrained by the circle defined by $\Re\{z^{\mathrm{L}}\} = 0$. Every z^{R} within this circle can be achieved (left). Using the constrained set of loads at the Tag reduces the minimum distance between constellation points compared to the full, unconstrained range (right). An optimal set of loads picked for one channel (GW1 @ 228 kHz) performs significantly worse on other channels (bottom).

so that the Tag can be used in various channels without manual adaption. In Figure 16 (bottom) we fitted a Moebius transformation to match the observed z^{R} and calculated the load impedances to yield optimal constellation points. We then compared the minimum distance with optimal constellation, with fixed loads (picked optimal for the first channel), and with the constrained loads from our Tag. We observe, that the constrained loads perform very similar to the fixed loads in most channels. Channel GW2 at 228 kHz is an exception, where the fixed loads perform particularly bad, and the dynamic loads from our Tag perform significantly better, achieving a 35 % larger minimum distance when picking 2 symbols, and a 67 % larger distance at 4 symbols. The presented results suggest that even on the same structure and with the same type of transducer and in the same narrow frequency range, the channels have a significant influence on optimal load choice. However, the evidence does not show that dynamic loads dominate fixed loads or vice versa.

The channel model presented in Sect. 3 predicts the transformation from load to observed samples. To validate the feasibility of the model we first perform the load-picking algorithm presented in Sect. 4.3.2, which determines the

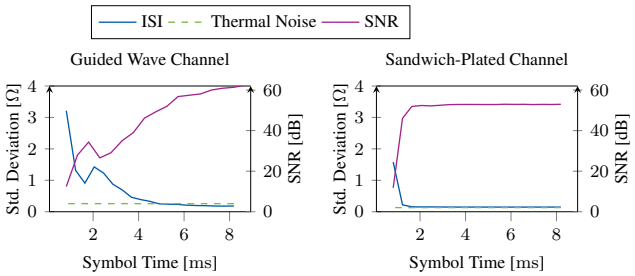

Figure 17: Thermal noise, ISI, and SNR development depending on symbol duration in a GW channel with $f_c \approx 200$ kHz, and in a SWP channel with $f_c \approx 1$ MHz. The ISI shrinks exponentially with symbol time.

transform from three measured points. We then compare the predicted constellation points with actual measurements, as illustrated in Figure 12 (right). On average over all channels, the deviations between predicted and measured z^{R} is just 3.9 mV with very little variance between the channels (maximum 6.1 mV, minimum 2.7 mV). This is merely 4.0 % of the minimum distance between constellation points, when picking the best 4 symbols in these channels. Naturally, the prediction error becomes more significant, when the minimum distance between samples is reduced. When picking 16 symbols the relative error rises to 34 % on average.

As the cause of these deviations between prediction and measurement, we suspect 1) non-ideal behavior of components, such as inductors and capacitors, 2) noisy measurement of the base points the Moebius transform is calculated from, and 3) simplifications of the equivalent circuit, that is used as a basis for the prediction.

5.4 Transient and Measurement Noise

During communication, two distinct types of errors arise: Thermal noise is introduced, e. g., by the analog circuits and during the ADC conversion, while inter-symbol interference (ISI) is introduced by the multipath characteristics of the channel. The magnitude of both types is shown in Fig. 17 for a GW and an SWP channel. The thermal noise was measured while the Tag did not modulate the signal, while the ISI curve shows the average deviation of the observed samples from the expected constellation point in 200 messages.

Inter-symbol interference is exponentially falling when longer symbol durations are chosen, which is a direct consequence of the exponential attenuation of waves in metal. However, the SWP-channel has a significantly stronger attenuation than the GW-channel, resulting in less ISI. This shows that the main limitation for higher data rates is ISI with shorter symbol-times, and it shows that ISI is much more problematic in GW than in SWP channels.

5.5 Transmission Speed and Reliability

We explore the achievable data rates of the proposed communication scheme with various parameters. For this evaluation, we transmit pseudo random messages from Tag to Reader and calculate the bit-error-rate (BER) and packet error rate (PER) with each set of parameters. For all channels and all sets of symbols, we used the automated procedure described in Sect. 4 to derive frequency and load impedances, without manual tweaking. For every setup, 200 messages with 576 bits per message were transmitted.

If binary load modulation is used, the difference between observed states is maximal and hence, shorter symbol times may be possible. We evaluate the effective gain of using higher-order modulation by comparing the highest achievable data rate with the presented modulation scheme against the achievable data rate with binary modulation. A data rate is defined achievable, if it is possible to transmit messages with a packet error rate less than or equal to one percent. Figure 19 shows the largest achievable data rates for all channels with different numbers of symbols. As a comparison, we have also implemented a binary modulation scheme.

The results show that binary modulation is in no case the optimal choice. However, the gain of using higher-order modulation strongly depends on the channel: The SWP channel achieves a 211 % increase in data rate, while the GW channels only achieve between 13 and 66 % increase when using higher order modulation. The shorter delay spread (see Fig. 3 and Sect. 5.4) enables short symbol times with little ISI, even when many symbols are used, i. e., the distance between constellation points is small. In GW channels, in contrast, reduced symbol time strongly increases ISI, which complicates the accurate discrimination of close constellation points.

Figure 19 also compares the highest achievable data rates without channel coding. As for all measurements, we have used an LDPC code from the IEEE 802.16 (WiMAX) standard with code-rate $R = 0.83$. The code was retrieved from [12]. In binary modulation, the uncoded communication achieves in some cases even higher data rates than the one with channel coding, where the same short symbol time could be achieved without coding and no parity bits have to be included in the message. Higher-order modulation, however, has only been advantageous in our tests when combined with error correcting channel coding.

Among the GW channels, the effect of distance between the transducers is not conclusive. While the largest distance (3 m in GW3) achieves only half the data rate compared to GW1 and GW2, the 2 m channel (GW2) achieves equal performance as the 1 m channel (GW1). For other acoustic channels, such as the acoustic underwater channel, it has been shown that geometry plays a dominant role for shorter distances [23], which is likely also the case here. However,

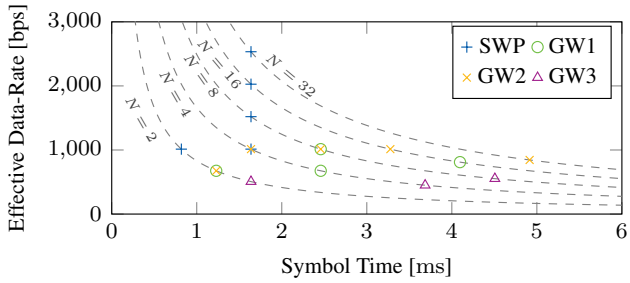

Figure 18: Because of varying delay spreads, different symbol times and data rates could be achieved in the channels under tests. The figure shows only the shortest feasible symbol time for every channel and every number of symbols.

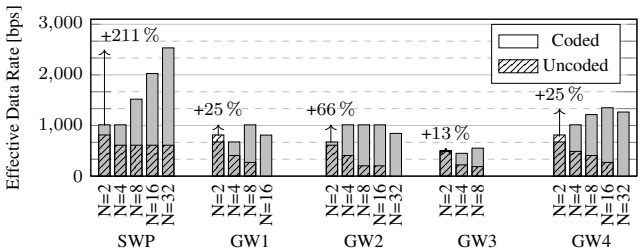

Figure 19: Comparison of the highest achievable data rates with higher-order load modulation compared to simple binary modulation over different channels. Higher order modulation only increased data rates in combination with channel coding.

in all channels under test, reliable, i. e., error free communication has been possible.

5.6 Refined Channel Estimation

In Sect. 4.4.2, we presented an approach to correct the estimated chanel constellation points. In this experiment, we perform a channel estimation once to establish the mapping between z^{L} and z^{R}, and then start to send one message with randomized content per second for 1000 s. We compare the received and decoded messages and count the number of bit errors. The bit errors of every ten consecutive messages are averaged to smooth out random fluctuations.

Figure 20 shows the bit errors per message over time. After a fresh channel estimation, both approaches perform well, and all bits are decoded correctly. After approximately 300 seconds, however, the Reader without refined channel estimation starts to show increasing bit error rates and becomes unusable. At the same time, the preamble correction approach keeps the same low bit error rate constant during the whole experiment duration of roughly 16 minutes. Hence, without using the preamble for correcting channel

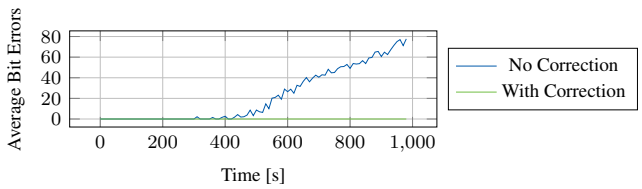

Figure 20: Bit Errors in messages over time with and without the refined channel estimation. For this experiment, 32 symbols were used, and the symbol duration was 5 ms

.

variations, the full channel estimation would have to be repeated more often, reducing the effective data rate of the system significantly. Similar results have been reproduced for all tested channels.

6 DISCUSSION

Higher-order load modulation schemes increase achievable data rates, but come at a cost: Tags require multiple bulky inductors and switches, while the Reader has to calculate the amplitude and phase of the incoming signal. In contrast, binary modulation just requires an envelope detector at the Reader, and a transistor at the Tag. However, at least one inductor for impedance matching is required in all cases. Optimizations are viable for the Tag and Reader to reduce size and complexity, e. g., the Tag could use just a single inductor and a bank of capacitors in series, which enables smaller form factors, and the Reader could implement hardware-based homodyne phase and amplitude detection.

Unfortunately, prior work is very heterogenous: most research groups used their own custom hardware, which we did not have access to[1]. Piezo transducers and specimen material and geometry were also different. Our results in the SWP channel are well in line with the 2.7 kbit s^{-1} reported in [6], although the piezo transducers used in our experiments had only about one fifth of the size. For GW channels, no prior work on passive communication exists. In our experiments, higher-order modulation raised the data rates between 13 and 66 % in GW channels in combination with channel coding.

The achievable data rates are limited by multipath propagation in metal channels, which is conventionally mitigated by channel equalization. The nonlinearity of the backscatter channel complicates the implementation of straightforward equalization techniques, such as symbol-by-symbol equalizers. In future work, backscatter channel equalization could strongly increase the potential of acoustic backscatter communication. Furthermore, in the scope of this work, we only investigated a single coding scheme (LDPC). Future work should provide a detailed analysis of tradeoffs between coding gain and performance for different coding schemes.

A major advantage of backscatter communication is the reduced energy demand of the Tag. Our Tag prototype was designed as a proof of concept, and is not optimized for low-power consumption. However, we can provide a rough estimate of the required power. The power-consuming parts in the Tag are the switch, the potentiometer, and an MCU. The potentiometer consumes, according to its datasheet, about 1 μA, and switches with low on-state resistance, e. g., the ADG811 consume on average another 1 μA. Because of the low data rates, a simple MCU can be used and can spend most of the time in sleep mode during message transmission. Assuming a simple 8-bit low-power MCU such as the PIC18F K40 from Microchip Technology spending 99 percent of the time in sleep mode[2], it is reasonable to expect a total current drain of less than 4 μA at a 2.7 V supply voltage. With a data rate of 1 kbit s^{-1}, the required energy is roughly 13.5 nJ per information bit. Compared to other communication technologies, this is in the range of the power requirement for Bluetooth Low-Energy (BLE), e. g. [19], but still orders of magnitude higher than electromagnetic backscatter technologies. In any case, power harvesting of 470 mW in GW channels over short distances [31] and of 250 mW through SWP channels [28] have been demonstrated, which provide more than enough energy for the Tag.

In future work, an important step is to integrate the presented communication scheme with acoustic energy transfer and a forward-link to complete a full RFID-like system. This will be a challenge because the choice of load impedance at the Tag will influence the harvested energy, which has to be considered when picking loads.

7 CONCLUSION

This work shows that acoustic backscatter communication is not only feasible in sandwich-plated channels, but also in guided-wave metal channels, which has not been demonstrated to date. Reliable communication was achieved in this type of channel, covering distances up to 3 m. The potential of using dynamic carrier frequencies and load selection was demonstrated.

We presented the design of a custom Tag hardware, allowing to switch the electric load at its transducer to a large variety of different impedances, and a Reader, that can perform up to 2500 impedance measurements per second on its transducer. The schematics and PCB layouts of the hardware will be published open-source upon publication.

[1] We will publish our circuits and PCB layouts upon publication

[2] Assuming a symbol duration of 1 ms, the MCU must set the poti and switch via an I2C command per symbol, which takes less than 10 µs active time every millisecond.

By deriving and evaluating a channel model for the acoustic backscatter channel based on Moebius transforms, we enabled dynamic choice of optimal loads for higher-order load modulation schemes, which increased the data rates in acoustic backscatter systems in all our tests—both in SWP and GW-channels—compared to binary modulation. In the best test case, 211 % increase in data rate was achieved. However, the strongest gains in higher-order load modulation were only achieved in combination with channel coding. A novel technique was used to leverage the preamble as a training sequence to compensate for slight channel variations without having to perform regular channel estimation.

REFERENCES

[1] Sayed Saad Afzal, Reza Ghaffarivardavagh, Waleed Akbar, Osvy Rodriguez, and Fadel Adib. 2020. Enabling Higher-Order Modulation for Underwater Backscatter Communication. In *Global Oceans 2020: Singapore–US Gulf Coast*. IEEE.

[2] J. M. Algueta-Migue, J. R. Garcí a Oya, A. J. LÓpez-Martin, C. A. De La Cruz Blas, F. Muñoz Chavero, and E. Hidalgo-Fort. 2019. Low-Power Ultrasonic Front-End for Cargo Container Monitoring. *IEEE Transactions on Instrumentation and Measurement* (2019), 1–1.

[3] Jonathan D. Ashdown, Kyle R. Wilt, Tristan J. Lawry, Gary J. Saulnier, David A. Shoudy, Henry A. Scarton, and Andrew J. Gavens. 2013. A full-duplex ultrasonic through-wall communication and power delivery system. *IEEE Transactions on Ultrasonics, Ferroelectrics, and Frequency Control* 60, 3 (March 2013), 587–595.

[4] C. Bacher, P. Palensky, and S. Mahlknecht. 2005. Low cost data transmission via metallic solids for sensor networking. In *Proceedings of the IEEE Symposium on Emerging Technologies, 2005*. 193–198.

[5] J. Bok and H. Ryu. 2012. Mitigation of multipath in steel wall channel of ultrasonic communication system. In *2012 International Conference on ICT Convergence (ICTC)*. 449–453.

[6] Michael T Cunningham, Gary J Saulnier, Robert Chase, Edward M Curt, Kyle R Wilt, Francisco J Maldonado, Stephen Oonk, and Henry A Scarton. 2016. Low-rate ultrasonic communications and power delivery for sensor applications. In *MILCOM 2016-2016 IEEE Military Communications Conference*. IEEE, 91–96.

[7] Falko Dressler and Stefan Fischer. 2015. Connecting in-body nano communication with body area networks: Challenges and opportunities of the Internet of Nano Things. *Nano Communication Networks* 6, 2 (2015), 29–38.

[8] Mohammad Meraj Ghanbari and Rikky Muller. 2020. Optimizing Volumetric Efficiency and Backscatter Communication in Biosensing Ultrasonic Implants. *IEEE Transactions on Biomedical Circuits and Systems* 14, 6 (Dec. 2020), 1381–1392. Conference Name: IEEE Transactions on Biomedical Circuits and Systems.

[9] D. J. Graham, J. A. Neasham, and B. S. Sharif. 2011. Investigation of Methods for Data Communication and Power Delivery Through Metals. *IEEE Transactions on Industrial Electronics* 58, 10 (Oct. 2011), 4972–4980.

[10] Raffaele Guida, Neil Dave, Francesco Restuccia, Emrecan Demirors, and Tommaso Melodia. 2019. U-Verse: a miniaturized platform for end-to-end closed-loop implantable internet of medical things systems. In *Proceedings of the 17th Conference on Embedded Networked Sensor Systems*. 311–323.

[11] Alexander Heifetz, Jafar Saniie, Xin Huang, Boyang Wang, Dmitry Shribak, Eugene R Koehl, Sasan Bakhtiari, and Richard B Vilim. 2019. *Final Report for Transmission of Information by Acoustic Communication Along Metal Pathways in Nuclear Facilities*. Technical Report. Argonne National Lab.(ANL), Argonne, IL (United States).

[12] Michael Helmling, Stefan Scholl, Florian Gensheimer, Tobias Dietz, Kira Kraft, Stefan Ruzika, and Norbert Wehn. 2019. Database of Channel Codes and ML Simulation Results. www.uni-kl.de/channel-codes. (2019).

[13] Thomas Hosman, Mark Yeary, John K Antonio, and Brent Hobbs. 2010. Multi-tone FSK for ultrasonic communication. In *2010 IEEE Instrumentation & Measurement Technology Conference Proceedings*. IEEE, 1424–1429.

[14] X. Huang, J. Saniie, S. Bakhtiari, and A. Heifetz. 2018. Applying EMAT for Ultrasonic Communication Through Steel Plates and Pipes. In *2018 IEEE International Conference on Electro/Information Technology (EIT)*. 0379–0383.

[15] Junsu Jang and Fadel Adib. 2019. Underwater backscatter networking. In *Proceedings of the ACM Special Interest Group on Data Communication*. 187–199.

[16] Marina Jordão, Ricardo Correia, and Nuno Borges Carvalho. 2019. Characterisation and implementation of high-order backscatter modulation for IoT applications. *IET Microwaves, Antennas & Propagation* 13, 15 (2019), 2636–2640.

[17] M. Kluge, Th. Becker, J. Schalk, and T. Otterpohl. 2008. Remote acoustic powering and data transmission for sensors inside of conductive envelopes. In *2008 IEEE SENSORS*. 41–44. ISSN: 1930-0395.

[18] Hartmudt Koeppe, Sven Thamm, Thomas Trettin, Ulrike Steinmann, and Joerg Auge. 2014. A wireless supplied multi-sensor-system for spatial resolved inline process analysis. In *Sensors and Measuring Systems 2014; 17. ITG/GMA Symposium*. 1–5.

[19] Yao-Hong Liu, Christian Bachmann, Xiaoyan Wang, Yan Zhang, Ao Ba, Benjamin Busze, Ming Ding, Pieter Harpe, Gert-Jan van Schaik, Georgios Selimis, Hans Giesen, Jordy Gloudemans, Adnane Sbai, Li Huang, Hiromu Kato, Guido Dolmans, Kathleen Philips, and Harmke de Groot. 2015. 13.2 A 3.7mW-RX 4.4mW-TX fully integrated Bluetooth Low-Energy/IEEE802.15.4/proprietary SoC with an ADPLL-based fast frequency offset compensation in 40nm CMOS. In *2015 IEEE International Solid-State Circuits Conference - (ISSCC) Digest of Technical Papers*. 1–3. https://doi.org/10.1109/ISSCC.2015.7063013

[20] Peter Oppermann and Christian Renner. 2019. Low-Power Ultrasonic Wake-Up and Communication through Structural Elements. In *Proceedings of the 7th International Workshop on Energy Harvesting & Energy-Neutral Sensing Systems (ENSsys'19)*. Association for Computing Machinery, New York, NY, USA.

[21] Enrico Paolini and Mark Flanagan. 2014. Low-Density Parity-Check Code Constructions. In *Channel Coding*, David Declerq, Marc Fossorier, and Ezio Biglieri (Eds.). Academic Press, Oxford, 141–209.

[22] Dominique Paret. 2009. *RFID at ultra and super high frequencies*. Wiley.

[23] Bernd-Christian Renner, Jan Heitmann, and Fabian Steinmetz. 2020. ahoi: Inexpensive, Low-power Communication and Localization for Underwater Sensor Networks and μAUVs. *ACM Transactions on Sensor Networks (TOSN)* 16, 2 (2020), 1–46.

[24] Richard Primerano, Moshe Kam, and Kapil Dandekar. 2009. High bit rate ultrasonic communication through metal channels. In *2009 43rd Annual Conference on Information Sciences and Systems*. 902–906. https://doi.org/10.1109/CISS.2009.5054845

[25] Sebastian Roa-Prada, Henry A. Scarton, Gary J. Saulnier, David A. Shoudy, Jonathan D. Ashdown, Pankaj K. Das, and Andrew J. Gavens. 2013. An Ultrasonic Through-Wall Communication (UTWC) System Model. *Journal of Vibration and Acoustics* 135, 1 (02 2013).

[26] M. G. L. Roes. 2015. *Exploring the potential of acoustic energy transfer*. Ph.D. Dissertation. https://research.tue.nl/en/publications/exploring-the-potential-of-acoustic-energy-transfer

[27] G. J. Saulnier, H. A. Scarton, A. J. Gavens, D. A. Shoudy, S. Bard, S. Roa-Prada, T. L. Murphy, M. Wetzel, and P. Das. 2006. *Through-Wall Communicatin of Low-Rate Digital Data Using Ultrasound*. Technical Report LM-06K102. Knolls Atomic Power Laboratory (KAPL), Niskayuna, NY.

[28] D. A. Shoudy, G. J. Saulnier, H. A. Scarton, P. K. Das, S. Roa-Prada, J. D. Ashdown, and A. J. Gavens. 2007. P3F-5 An Ultrasonic Through-Wall Communication System with Power Harvesting. In *2007 IEEE Ultrasonics Symposium Proceedings*. 1848–1853.

[29] Zhongqing Su. 2009. *Identification of Damage Using Lamb Waves*. Springer London.

[30] Victor Farm-Guoo Tseng, Sarah S. Bedair, and Nathan Lazarus. 2018. Acoustic Power Transfer and Communication With a Wireless Sensor Embedded Within Metal. *IEEE Sensors Journal* 18, 13 (July 2018), 5550–5558. https://doi.org/10.1109/JSEN.2018.2839558

[31] Victor Farm-Guoo Tseng, Sarah S. Bedair, Joshua J. Radice, Trevon E. Drummond, and Nathan Lazarus. 2020. Ultrasonic Lamb Waves for Wireless Power Transfer. *IEEE Transactions on Ultrasonics, Ferroelectrics, and Frequency Control* 67, 3 (March 2020), 664–670. https://doi.org/10.1109/TUFFC.2019.2949467

[32] S. Yang and A. C. Singer. 2016. Energy Efficient Ultrasonic Communication on Steel Pipes. In *2016 IEEE International Workshop on Signal Processing Systems (SiPS)*. 297–302.

[33] Lonzhi Yuan, Can Xiong, Si Chen, and Wei Gong. 2021. Embracing Self-Powered Wireless Wearables for Smart Healthcare. In *2021 IEEE International Conference on Pervasive Computing and Communications (PerCom)*. 1–7. https://doi.org/10.1109/PERCOM50583.2021.9439117

[34] Jianing Zhang, Ziying Yu, Hengxu Yang, Ming Wu, and Jun Yang. 2015. Wireless communication using ultrasound through metal barriers: Experiment and analysis. In *2015 10th International Conference on Information, Communications and Signal Processing (ICICS)*. 1–5.